A Rectangular End-Winding Model for Enhanced Circulating Current Prediction in AC Machines

Frederic Maurer and Jonas Kristiansen Nøland, *Member, IEEE*

***Abstract*—The end-winding region is usually overlooked in the roebel design of large AC machines. However, saturated stator slots cause overhang parts to impact the circulating currents significantly. In fact, a precise knowledge of the winding overhang strand inductances is crucial when optimising the transpositions of large roebel bars, especially in the case of under-roebeling (having less than 360-transposition in the active part) where the goal is to compensate the winding overhang parasitic field with the slot-parasitic field. In this paper, a rectangular inductance calculation model (R-ICM) is proposed. It results in a circuital lumped-element model (LEM) that takes the strand dimensions, the bar bending, as well as small-scale effects into account. Moreover, the work describes how to model finite current-carrying rectangular segments (straight and arced) from first principles. Finally, the methodology was demonstrated for two prototype specimens with different bending-shapes corresponding to the fundamental elements on a stator bar in the winding overhang of large electrical machines.**

***Index Terms*—Circulating currents, inductance calculation, machine overhang, end-winding, stator bars, roebel bars.**

I. Introduction

CIRCULATING currents are inevitably useless as they contribute to joule losses in electrical machines and are therefore a key challenge in winding design. These currents flow in a closed cycle between conducting bars that are separated into several parallel strands, which are used to reduce the eddy current losses in the conductors. However, the complexity in the calculation has been a major issue since their discovery.

The phenomenon was initially studied for turbo-generators in the 1970s, where there have been several cases of stator bar damages [1], [2]. The problem was mainly due to local overheating produced by circulating current losses. In the recent years, there have been plenty of efforts on the calculation, optimisation and detection of circulating currents in wide range of large AC machines [3]–[17]. The industry responded with patents for special transpositions that reduces these circulating current losses [18].

In order to improve the analysis of the stator armature, the strand slot-leakage reactance calculation has been proposed using analytical and numerical approaches [6]–[10]. In [15], a strand current measurement method based on a search coil was presented. Moreover, the finite element analysis (FEA) environment has been improved to include small-scale effects, transpositions, non-uniformities and inter-turn faults [19]–[24].

Manuscript received January 12, 2020; revised May 11, 2020; accepted July 12, 2020. Paper no. TEC-00035-2020. (*Corresponding author: Frederic Maurer.*)

F. Maurer is with the Swiss Federal Institute of Technology Lausanne.

J. K. Nøland is with the Norwegian University of Science and Technology, 7034 Trondheim, Norway (e-mail: jonas.k.noland@ntnu.no).

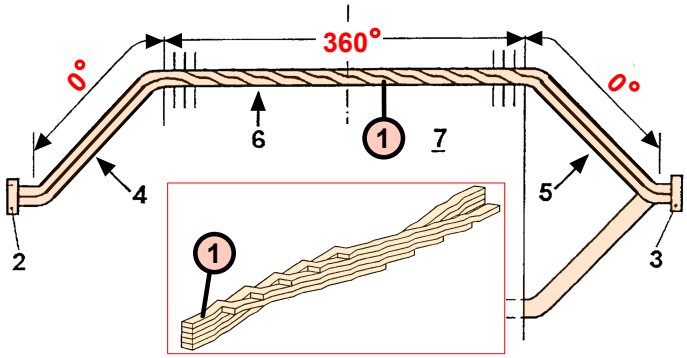

Fig. 1: Total winding through a stator slot of a large AC machine [25]. Segments 4 and 5 are under investigation herein.

Usually, the non-saturated strand inductances in the active part are factor 10-20 times bigger than in the overhang of large AC machines [25]. Such conditions exist during the stator short-circuit measurement according to the IEC60034 standard, or in the approach of [15]. However, in nominal conditions, the strand inductance ratio usually drops by a factor 5-7 for doubly-fed induction machines (DFIMs) when the stator slots are saturated [25]. As a result, the winding overhang strand inductance has a significantly stronger influence on the circulating currents. Therefore, one has to rely on a precise strand inductance model of the end-winding to compute circulating current losses in nominal conditions, and thus, avoid any damaged bar due to local overheating.

The present methods to compute the strand inductances are based on a 2-D filament approach [11]–[14], which takes neither the bar bendings nor the exact strand dimensions into account. The inductances should reflect the bar geometry data since the magnetic field has a significant impact in the vicinity of the strands [25]. Moreover, a uniform definition of the return conductor seems to be lacking. In this article, a detailed overhang strand inductance model based on the partial inductance (PI) concept is proposed to overcome these obstacles. Using PIs, there is no need to define a return conductor anymore [25], as the exact strand geometry is inserted.

This paper is validated on two small-scale specimens of the two fundamental strand models, i.e., the straight and the arced configurations (depicted in Fig. 2). They correspond to the fundamental parts of any roebel bar in the winding overhang (refer to segments 4 and 5 of Fig 1). In this

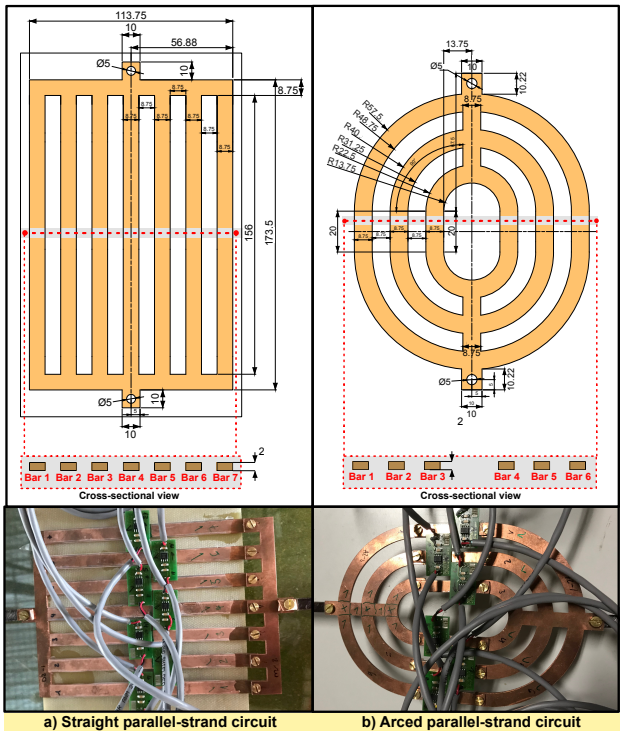

Fig. 2: Prototypes of two different parallel-strand circuits made of copper.

experimental setup, the space between the conductor needed to be increased in comparison to a standard roebel bar. In this way, there is enough space to place the hall-sensors, thus enabling non-invasive measurement. It is worth noting that a direct series-resistance current measurement method would have significantly influenced the results. In fact, a small-scale model enables the study of different phenomena, such as the impact of internal field (as in this paper). Moreover, one could study the impact of an external field (e.g., the rotor field) or of a magnetizable iron. Such flexibility could not be achieved using a full-scale model. The chosen small-scale configuration allows analysing each impact separately so that the models can be validated with high accuracy. In addition, the small-scale models can also identify small-scale effects that are negligible in a full-scale model.

II. Electromagnetic Model

Two different approaches are used to do the calculation of circulating currents in roebel bars; Namely, the direct calculation method (DCM) [26] and the inductance calculation method (ICM) [27]. In the DCM, a 3-D non-linear finite-difference (FD) calculation scheme is used to obtain the magnetic field at a given time, from which the circulating currents can be deduced. Induced voltages are computed for each time step, and they are used to solve a damper-bar type circuit with only resistive elements. In the ICM, the circulating currents are derived also solving a damper-bar type of circuit. It is composed by voltage sources (u_i), inductances ($L_{i,k}$[1]) and resistances, with elements that can be obtained from an analytical calculation or numerical field calculation [1], [2], [25]. The main advantage of the ICM is to be able to identify the coupling between the different branches in the winding overhang of AC machines.

There will be no induced voltage (u_i) as there is no external flux source that interacts with the specimens (emulating the end-winding). The experimental results will be accessed against both the filament model (FM) [1], [2] and the rectangular model (RM) [25], which is the proposed novel model. Both models are based on the ICM, but they differ by the underlying hypothesis on the conductor path. In the FM, the conductors are seen as infinite with zero cross-sections, as a 2D approach. In the RM, the conductors are fully modelled using their complete and exact 3D geometry, making only a hypothesis on a constant current density within their cross-section. We expect to get significantly better results over a wide range of geometries with the RM approach. It incorporates the exact geometry to better account for the electromagnetic problem. The RM was initially developed in [25], where it has been shown that the detailed dimensions of the branches have a significant impact on the inductance components. This is based on the concept of partial inductance (PI) [28]–[30], whereas the subdivision of the inductance loops into fundamental parts (refer to Sec. II-A3) is arbitrary and has no influence on the mutual inductance [25].

A. Inductance calculation methodology for the RM method

Fig. 3 outlines a simplified ICM procedure with straight parallel branches. The different steps needed and the employed equations are detailed in this subsection. The methodology feeds inductance parameters into the lumped-element model (LEM), which are detailed in the following subsection.

Consequently, the inductances (e.g., $L_{01,01}$, etc.) will be determined only on the branches as the branches will implicitly form loops as the circuit is closed to enable a current to flow. The inductances are computed using a 3D-volume iterative numerical quadrature scheme [25] to achieve a precision of around 100 times the machine precision on the computed inductances. Basically, the iterative numerical scheme is adjusting the number of sub-segments to be integrated as well as the order of the numerical quadrature until reaching the required numerical precision [25]. The inductance component L_{ik} (e.g., $L_{01,02}$) is computed using the following formula [31]

$$L_{i,k} = \frac{1}{I \cdot S_c} \int_{l_b} \iint_{S_c} (\vec{A}_{ik} \mathrm{d}S) \cdot \mathrm{d}\vec{l} \qquad (1)$$

where the integration is first done over the surface S_c of the conductor (2mm x 8.75mm) and then over its length (156mm for straight branches). The index i represents the source conductor, while k corresponds to the conductor where the vector potential is applied. Consequently, the self-inductance is calculated when $i = k$. For example, $L_{01,01}$ refers to

[1]The circuit could be further extended with the term $i_k \frac{d}{dt} L_{ik}$-term to take the inductance saturation into account [25].

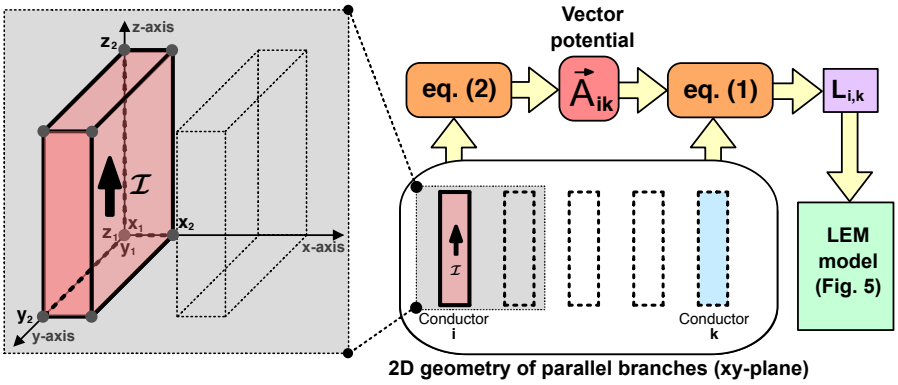

Fig. 3: A simplified inductance calculation procedure for straigh rectangular conductors in parallel (**i** is the source conductor)).

the self-inductance of branch 1, whereas $L_{11,11}$ is the self-inductance of branch 11 and so on. The integration over the surface ($\iint_{S_c}(\vec{A}_{ik}\mathrm{d}S)$) yields a prediction of the mean value of the vector potential over the strand surface and enables, therefore, to take the exact strand geometry into account.

The inductance components for the prototypes of Fig. 2 are found from analytical expressions for straight conductors, and arced conductors, which are detailed in the following paragraphs of this subsection, before the inductance calculation algorithm is described in the next subsection.

1) The Vector Potential from Straight Conductors: For a straight conductor parallel to the z axis, with cross-section $(x_2-x_1)\times(y_2-y_1)$ (x and y can be chosen arbitrary, for example 2mm x 8.75mm), length (z_2-z_1) (for example 156mm) and assuming a constant current density[2] in positive z direction[3], the vector potential formula for a unitary current can be taken from [32]. It is recalled hereafter that the vector potential originating from the current flowing in one individual branch to be

$$\begin{aligned} A_z(x,y,z) = \frac{\mu_0 I}{4\pi}\sum_{i,j,k=1}^{2}(-1)^{i+j+k}[&x_i y_j \operatorname{arcsinh}(\theta_1) \\ &+ y_j z_k \operatorname{arcsinh}(\theta_2) + z_k x_i \operatorname{arcsinh}(\theta_3) \\ &- \frac{1}{2}(x_i^2 \arctan(\theta_4) + y_j^2 \arctan(\theta_5) \\ &+ z_k^2 \arctan(\theta_6))] \end{aligned} \tag{2}$$

where $\theta_1 = \frac{z_k}{\alpha_{ij}}$, $\theta_2 = \frac{x_i}{\beta_{jk}}$, $\theta_3 = \frac{y_j}{\gamma_{ki}}$, $\theta_4 = \frac{y_j z_k}{x_i r}$, $\theta_5 = \frac{x_i y_j}{z_k r}$, with $\alpha_{ij}^2 = u_i^2 + v_j^2$, $\beta_{ij}^2 = v_i^2 + w_j^2$, $\gamma_{ij}^2 = w_i^2 + u_j^2$, $u_i = x_i - x$, $v_j = y_j - y$, $w_k = z_k - z$, $i,j,k = 1,2$ and I is the current of the conductor. Fig. 3 depicts the source conductor where the different geometrical indexes are applied to x, y and z coordinates.

2) The Vector Potential from Arced Conductors: In the case of an arced conductor oriented along the tangential axis, with a rectangular cross-section $(r_2-r_1)\times(z_2-z_1)$, length $(\phi_2-\phi_1)$ and assuming a constant current density[4] in positive tangential direction, the formula for the vector potentials can be taken from [25], [33], using a similar procedure as for straight conductors. Eq. (3) and eq. (27) of [33] yields A_r and A_φ, whereas the arched current density is in the φ-direction. The transformation between local and global coordinates makes both A_r and A_φ necessary for eq. (1).

3) Inductance calculation algorithm: The full geometry of the branched circuit must be known. The inductance calculation is done proceeding in the following way.

1) Divide the circuit into straight and arced parts, i.e., fundamental parts (refer to Figs. 2 and 5).
2) Define for each fundamental part in a local coordinate system, as the vector potential formulas of subsections II-A1 and II-A2 are given in local coordinates.
3) Define the coordinate transformation from the local coordinate system to the global coordinate system, where the inductances are computed.
4) Choose a conductor where the inductance must be computed and a source conductor.
5) Compute the inductance applying eq. (1) and using the adaptative numerical quadrature algorithm to achieve sufficient precision.
6) Repeat 4) and 5) until all individual inductance relationships between the branches have been computed.

B. Lumped-element model (LEM)

Once all inductances have been calculated, a circuit equation solver like SIMSEN[5] is used to compute the circulating currents. The circuit corresponding to the experimental setup (see Fig. 2a) is depicted in Fig. 5. This circuit is adapted accordingly for the second experimental setup (see Fig. 2b). The equivalent circuit is composed of 15 linked inductors. A 15x15 inductance matrix presented in Table I). The current source is modelled using a voltage source VS1 (with a sinusodal feeding at 50Hz) with a 1000kΩ series resistor R_1. The current feeding and return branch of the current can be neglected from the equivalent circuit. The experimental setup has been intentionally designed (long straight cables) to annul the impact of the feeding on the experiment.

At first glance, the computation model is composed of elements (straight bars) without considering the bar junctions

[2]In other words neglecting the skin effect.

[3]As the vector potential is linked to the current density by a laplacian-operator, they are co-linear.

[4]I.e., neglecting the skin effect.

[5]https://simsen.epfl.ch.

TABLE I: Straight circuit: Normalized inductance matrix for Fig. 5 with 0.126 μH base or 39.89 $\mu\Omega$ at 50Hz self-reactance. Self-inductances highlighted in bold. The chosen base represents the value of the highest inductance.

	L01*	**L02***	**L03***	**L04***	**L05***	**L06***	**L07***	**L08***	**L09***	**L10***	**L11***	**L12***	**L13***	**L14***	**L15***
L01*	**1.000**	0.497	0.348	0.271	0.222	0.188	0.1643	0.0040	0.0021	0.00151	0.0012	0.0038	0.0021	0.0015	0.0012
L02*	0.4977	**0.962**	0.498	0.348	0.271	0.222	0.1874	0	0	0	0	0	0	0	0
L03*	0.3476	0.498	**0.962**	0.498	0.348	0.271	0.2216	0	0	0	0	0	0	0	0
L04*	0.2705	0.348	0.498	**0.962**	0.498	0.348	0.2705	0	0	0	0	0	0	0	0
L05*	0.2216	0.270	0.348	0.498	**0.962**	0.498	0.3476	0	0	0	0	0	0	0	0
L06*	0.1874	0.222	0.271	0.348	0.498	**0.962**	0.4977	0	0	0	0	0	0	0	0
L07*	0.1646	0.188	0.222	0.271	0.349	0.499	**1.000**	0.0012	0.0015	0.0020	0.0038	0.0012	0.0015	0.0021	0.0038
L08*	0.0039	0	0	0	0	0	0.0012	**0.0180**	0.0035	0.0017	0.0012	0.0004	0.0004	0.0004	0.0004
L09*	0.0021	0	0	0	0	0	0.0015	0.0035	**0.0180**	0.0035	0.0017	0.0004	0.0004	0.0004	0.0004
L10*	0.0015	0	0	0	0	0	0.0021	0.0017	0.0035	**0.0180**	0.0035	0.0004	0.0004	0.0004	0.0004
L11*	0.0012	0	0	0	0	0	0.0039	0.0012	0.0017	0.0035	**0.0180**	0.0004	0.0004	0.0004	0.0004
L12*	0.0039	0	0	0	0	0	0.0012	0.0004	0.0004	0.0004	0.0004	**0.0180**	0.0035	0.0017	0.0012
L13*	0.0021	0	0	0	0	0	0.0015	0.0004	0.0004	0.0004	0.0004	0.0035	**0.0180**	0.0035	0.0017
L14*	0.0015	0	0	0	0	0	0.0021	0.0004	0.0004	0.0004	0.0004	0.0017	0.0035	**0.0180**	0.0035
L15*	0.0012	0	0	0	0	0	0.0039	0.0004	0.0004	0.0004	0.0004	0.0012	0.0017	0.0035	**0.0180**

TABLE II: Straight circuit: Normalized DC-resistive components for Fig. 4 with 210.405 $\mu\Omega$ base (with & without parasitic adds). An FEA study showed that the resistance increase due to eddy currents as well as proximity effect could be neglected due to the surrounding of air and the distance between conductors.

	R01	**R02**	**R03**	**R04**	**R05**	**R06**	**R07**	**R08**	**R09**	**R10**	**R11**	**R12**	**R13**	**R14**	**R15**
With adds	1.173	0.928	0.928	0.928	0.928	0.928	1.173	0.0793	0.0793	0.0793	0.0793	0.0793	0.0793	0.0793	0.0793
No adds	1.000	0.899	0.899	0.899	0.899	0.899	1.000	0.0504	0.0504	0.0504	0.0504	0.0504	0.0504	0.0504	0.0504

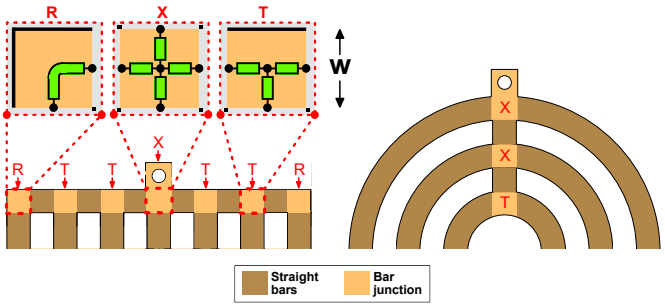

Fig. 4: Upper edge segment of the specimens indicating shaded areas for straight bars and bar junctions. Different junction segments (R,T and X) with their associated resistive parasitic networks are depicted.

depicted in Fig. 4, for the straight and the arc circuit, respectively. The figure illustrates an enhanced model adding resistive elements for the edges ("R" - 2 elements), T-crossings ("T" - 3 elements) and X-crossings ("X" - 4 elements). The cross-section of these ohmic resistances is equal to the cross-section of the rectangular conductor (w x h = 8.75 mm x 2.0 mm), while the individual parasitic lengths are given by the following expressions

$$l_R \approx \frac{w}{2} + \frac{1}{w}\int_0^w \frac{\pi}{2} r dr = \frac{w}{2} + \frac{\pi}{4} w = 11.247\,\text{mm}, \quad (3)$$

$$l_T \approx \frac{w}{2} = 4.375\,\text{mm}, \quad (4)$$

$$l_X \approx \frac{w}{2} = 4.375\,\text{mm}. \quad (5)$$

For parasitic length l_R, the whole edge length was considered (as indicated in Fig. 4). The mean arch length was calculated plus an additional experience-based length ($w/2$) added to take into account the non-uniform current density. The corner yields a mathematical singularity from an analytical point of view, i.e., the additional path length must be approximated numerically. For l_X, the numerical value corresponds to half of the conductor width (w). It postulates that a leading order of the equivalent resistance in the X-crossing is half of the conductor width. The same principle is applied for l_T. The resistance components with and without parasitic add-ons a depicted in Table II.

III. Experimental Calibration

The current measurements were indirectly obtained from special uniaxial hall sensors [6] (one per leg). The arrangement made non-invasive measurements possible. They convert the current-sourced magnetic fields into measurable voltages (by the hall effect). All the cables are twisted and shielded. Moreover, each hall sensor has a separate DC current source. The AC current measurement is indirect. As a result, the experimental precision is predicated on their calibration.

In the calibration process (identical for each circuit), each individual branches were fed with known AC sinusodal current (varying from 5A to 60A) at 50Hz. This was achieved practically by opening the screws and insulating the current from flowing in the other branches. In this way, the induced voltages in each branch are recorded. This information is gathered and utilized to obtain a vector that relates the coupling between a current of a branch and the voltage recordings of the hall sensor in all other branches. Repeating this step for all branches leads to an experimental transfer matrix, exhibiting the couplings in the circuit. As a result, the matrix can be used to compute the branch currents as a function of the measured induced voltages in the hall sensors (due to the linearity of the circuit).

[6] Melexis MLX91205 AAH-003 and AAL-003.

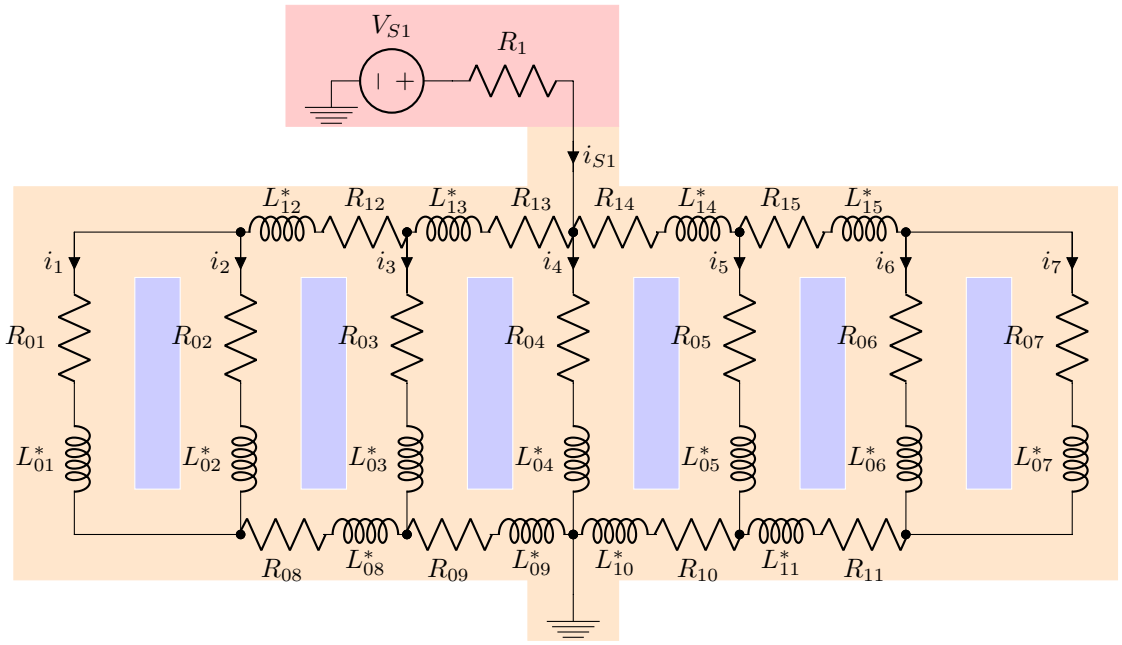

Fig. 5: Equivalent circuit of the prototype presented in Fig. 2a), where the mutual inductances are included in the inductors.

In a second step, the precision of the measurement is determined using an alternative circuit configuration and the experimental transfer matrix. The circuit presented in Fig. 5 is fed applying known AC-current into the branches 1 to 7, with some branches being isolated. First, the symmetrical branches 1 and 7 are fed exclusively. Then, branches 2 and 6, and branches 3 and 5, are fed in a similar way. Finally, branch 4 is fed, with all the others being isolated. The same procedure is done for the arced circuit, feeding branches 1 and 6, 2 and 5, and 3 and 4, respectively. It is reasonably postulated that the current ideally must be the same in each symmetric branch (constant current source). The results of the pairwise experiments are shown in tables III (for the straight circuit) and table IV (for the arced circuit). In fact, the current should be ideally zero for the isolated branches. The current amplitude should match with the one measured with a high-precision current probe. The differences between the probe and the ones computed using the transfer matrix and the hall sensors yield the measurement precision. Moreover, the threshold current can be determined from the maximal value of current calculated from the isolated branches.

For the straight circuit, the determined mean measurement precision is around 3.2% with the highest error for the hall sensor of leg number 7. The "threshold" current is around 1.5A, i.e., the maximum non-zero current obtained for the isolated branches yielding minimal current that can be determined using the indirect (non-invasive) current measurement method.

For the arced circuit, there are two outliers with a significant error (one overestimation and one underestimation). The mean precision is about 3.1% for all results. It should be noted that the threshold current is about 2.5A, i.e., higher than for the straight circuit. In fact, the arc portion has a negative impact on the magnetic field sensed by the hall sensors. The impact can only be partially removed by the calibration process.

It is very important to notice that the main goal of the calibration process it helps to remove the impact of the not perfectly aligned circuits and hall sensors as well as any other external impact on the measurement.

TABLE III: Straight circuit (depicted in Fig. 2a) : Pairwise cross-check of symmetrical branch currents I_1 & I_7, I_2 & I_6, I_3 & I_5 and I_4 (other legs isolated) against injected current I_{tot}.

Parameter	**Legs 1 & 7**	**Legs 2 & 6**	**Legs 3 & 5**	**Leg 4**
$\mathbf{I_1}$	**33.844 A**	1.393 A	1.333 A	1.470 A
$\mathbf{I_2}$	0.530 A	**31.794 A**	0.508 A	0.457 A
$\mathbf{I_3}$	0.167 A	0.168 A	**30.144 A**	0.179 A
$\mathbf{I_4}$	1.217 A	1.326 A	1.617 A	**57.623 A**
$\mathbf{I_5}$	1.054 A	0.834 A	**30.152 A**	1.278 A
$\mathbf{I_6}$	0.680 A	**31.357 A**	0.795 A	0.721 A
$\mathbf{I_7}$	**30.625 A**	0.228 A	0.084 A	0.042 A
$\mathbf{I_1 + .. + I_7}$	68.127 A	67.100 A	64.633 A	61.770 A
$\mathbf{I_{tot}}$ (injected)	65.523 A	64.549 A	62.473 A	58.314 A
$\mathbf{I_{tot}/2}$	32.762 A	32.275 A	31.237 A	58.314 A
Error 1st leg	+3.303%	-1.489%	-3.498%	-1.185%
Error 2nd leg	-6.523%	-2.843%	-3.472%	

IV. Main Results

The objective of the small-scale experiments was to assess the resistive effects from the current magnitudes and the inductive effects from the phase shifts between the strand currents fed with a sinusodal current source at 50Hz. Both circuits were made of copper, and they were surrounded by air (linear environment), implying a reduced inductive effect. As a result, both inductive and resistive effects could be observed in the model assessment. The remainder of this section presents the main experimental results and validations.

TABLE IV: Arced circuit (depicted in Fig. 2b): Pairwise cross-check of symmetrical branch currents I_1 & I_6, I_2 & I_5 and I_3 & I_4 (other legs isolated) against injected current I_{tot}.

Parameter	Legs 1 & 6	Legs 2 & 5	Legs 3 & 4
$\mathbf{I_1}$	**32.572 A**	1.397 A	1.199 A
$\mathbf{I_2}$	1.152 A	**28.774 A**	1.318 A
$\mathbf{I_3}$	1.546 A	1.470 A	**30.799 A**
$\mathbf{I_4}$	1.859 A	1.972 A	**30.586 A**
$\mathbf{I_5}$	2.150 A	**30.665 A**	1.923 A
$\mathbf{I_6}$	**29.691 A**	2.470 A	2.471 A
$\mathbf{I_1 + .. + I_6}$	66.820 A	66.748 A	68.296 A
$\mathbf{I_{tot}}$ (injected)	63.661 A	61.192 A	62.411 A
$\mathbf{I_{tot}/2}$	31.830 A	30.596 A	31.205 A
Error 1st leg	+2.331%	-5.955%	-1.301%
Error 2nd leg	-6.720%	+0.225%	-1.984%

A. *Validation of the Circuital Model*

First, a one-half period of the simulated current (with and without resistive adds) is assessed against the measurements. Theoretically, one would expect that the currents in branches 1 and 7, 2 and 6, and 3 and 5 to be the same. Fig. 6 shows excellent agreement for branches 2, 4, 5 and 6. However, there are more discrepancies for branches 1, 3 and 7. Fig. 7 depicts that six branch currents out of seven are within the measurement tolerances when using the additional parasitic resistances in the model. Only branch 4 remains outside. In fact, the measured currents seem to be in the middle of both models.

It must be stated that the presented measurement is nothing else than a short-circuit measurement where any piece of resistance and inductance will heavily influence the result. It is therefore straightforward that even small parametric errors in the model will have a significant impact on the calculated values. The additional parasitic resistances in the computational model improved the predictability, without clearing out all possible errors. In fact, the T-crossings (refer to the "T" in Fig. 4) cannot be modelled in detail using the LEM circuit. As a result, a smaller precision cannot be achieved for this particular crossing with the accessible LEM methodologies.

B. *Model Sensitivity to the Current Feeding Point*

There is a need to do a richer sensitivity study of the model against experiments, to highlight all possible mismatches. Therefore, an additional measurement series have been performed, modifying the location of the current feeding point. Fig. 5 depicts the circuit when the current is fed in and out of the nodes associated with leg 4 (center node). Alternatively, the nodes of legs 2, 3, 5 and 6 have been tested as feeding points as well. The study was performed using current clamps to change the current feeding location. The results of these measurements are shown in Table V. The precision (1.5A) causes the legs with the least current to have the highest error. As a result, some extreme cases occurred for some of the non-symmetrical test (feeding nodes of leg 2 or leg 3). However, the biggest errors were not exceeding the measurement precision (found in Sec. III). For the other branches, it seems that there is a correlation

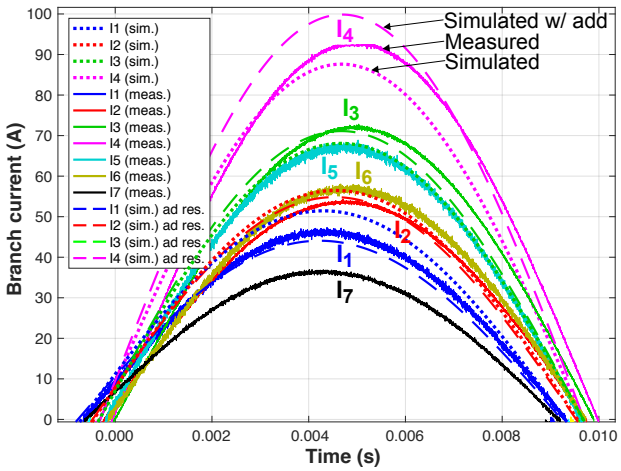

Fig. 6: Straight circuit (depicted in Fig. 2a): Time series of branch current. Due to symmetry reasons, fewer simulated currents are plotted (for example I1=I7 and so on).

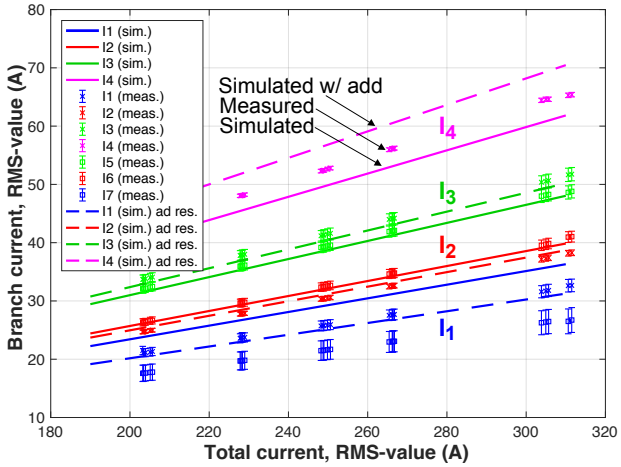

Fig. 7: Straight circuit: Branch current vs. Total current. Due to symmetry reasons, fewer simulated currents are plotted, since I1=I7 and so on).

between the feeding branch and an error minimum (taking the measurement error into account), which could be interpreted as a positive sign that supports the proposed T- and X-crossing add-on to the LEM model resistive components (as highlighted in Fig. 3 and Table II).

C. *The proposed RM vs. the FM*

Fig. 8 depicts the calculated branch currents using the FM and compares with the values from the RM developed in this paper. The currents computed with the FM present no symmetry since distance with respect to the return conductor has no symmetry; thus, the inductances are asymmetric as well as the currents. In addition, the return conductor is arbitrarily placed near conductor 1 (8.75mm to the left of conductor 1, same y coordinate and length as conductor 1). As a result, the value predicted for this branch is far away from reality. Similarly, if the return conductor would have been placed near another conductor, then the current of the nearest

TABLE V: Straight circuit: Sensitivity to the current feeding location on the model error (highest branch current highlighted).

Para-meter	Location	Leg 2		Leg 3		Leg 4		Leg 5		Leg 6	
		Value	Error	Value	Error [%]	Value	Error	Value	Error	Value	Error
$\mathbf{I_1}$	Simulated	13.357 A	-5.65%	9.106 A	-12.07%	6.276 A	-14.71%	4.562 A	-13.63%	3.643 A	-17.65%
	Measured	14.157 A		10.356 A		7.358 A		5.282 A		4.424 A	
$\mathbf{I_2}$	Simulated	**16.810 A**	**+4.79%**	11.405 A	-0.96%	7.809 A	+0.88%	5.608 A	+6.15%	4.430 A	+7.65%
	Measured	**16.042 A**		11.515 A		7.741 A		5.283 A		4.115 A	
$\mathbf{I_3}$	Simulated	11.296 A	-0.97%	**14.864 A**	**+5.17%**	10.128 A	-3.30%	7.211 A	+0.68%	5.652 A	+0.37%
	Measured	11.407 A		**14.133 A**		10.474 A		7.162 A		5.631 A	
$\mathbf{I_4}$	Simulated	7.759 A	-5.69%	10.183 A	-4.72%	**14.221 A**	**+2.85%**	10.075 A	-5.80%	7.856 A	-7.94%
	Measured	8.227 A		10.687 A		**13.827 A**		10.695 A		8.534 A	
$\mathbf{I_5}$	Simulated	5.581 A	+5.22%	7.289 A	+2.46%	10.129 A	-1.50%	**14.709 A**	**+5.08%**	11.436 A	+0.16%
	Measured	5.304 A		7.114 A		10.283 A		**13.998 A**		11.418 A	
$\mathbf{I_6}$	Simulated	4.375 A	+0.14%	5.668 A	+1.40%	7.815 A	6.14%	11.286 A	-9.15%	**17.018 A**	**+0.42%**
	Measured	4.369 A		5.590 A		8.326 A		12.423 A		**16.946 A**	
$\mathbf{I_7}$	Simulated	3.605 A	+65.14%	4.613 A	+41.59%	6.287 A	+12.21%	9.014 A	+7.25%	13.518 A	+8.40%
	Measured	2.183 A		3.258 A		5.603 A		8.405 A		12.471 A	
$\mathbf{I_{tot}}$	Simulated	62.783 A	+0.32%	63.128 A	+0.23%	62.665 A	+0.16%	62.465 A	+0.22%	63.553 A	+0.31%
	Measured	61.689 A	-1.43%	62.653 A	-0.53%	63.612 A	+1.67%	63.248 A	+1.48%	63.539 A	+0.29%
	Injected	62.583 A		62.984 A		62.565 A		62.327 A		63.357 A	

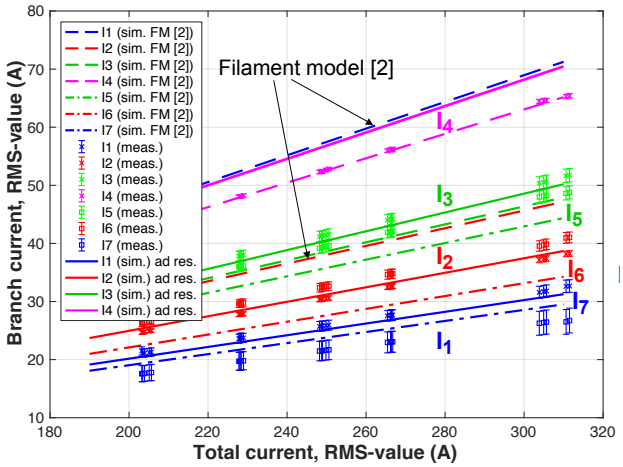

Fig. 8: Straight circuit: Branch current vs Total current in comparison with filament model (FM) [2] with this study.

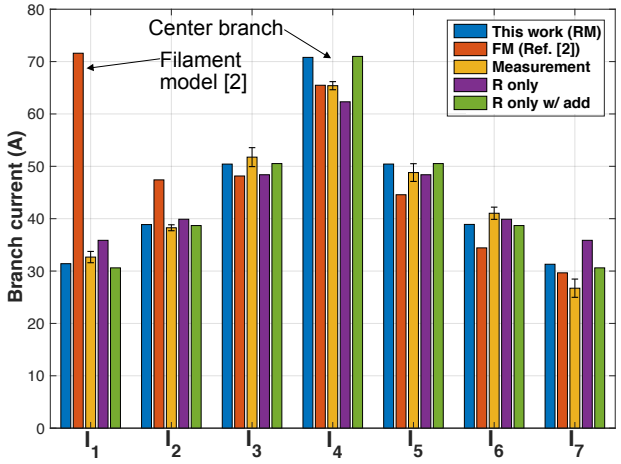

Fig. 9: Straight circuit: Bar graph of the branch current amplitude, comparison between different models.

conductor would have been wrong too. On the other hand, it is not practical to adjust the position of the return conductor in order to minimize the error between the measurements and the model. This is the main drawback of the FM, i.e., the position of the return conductor. The FM is less suitable because it lacks precision. It was initially introduced without any validation [1], [2]. The maximal FM value of the inductance (0.817 μH or 256.6$\mu\Omega$ at 50Hz) is about 6.5 times higher than for the RM model, which influences the error in the current distribution. It is the root cause of the non-symmetry observed in the branch currents. Again, one would expect to have currents to be mainly directed by resistive contribution. In fact, the measurement is nothing else than a short-circuit current measurement. However, any piece of impedance will impact the currents even more as the branches are in parallel to each other. Moreover, the inductances influence the phase angle of each branch current, which impacts the overall behaviour of the winding overhang.

The presented problems with the FM approach is avoided by the RM presented in this paper. As seen, only three currents agree with the measurements using the FM. The predictability is below the best case using the RM. Due to its symmetry problem, the FM has not been enhanced to take the edge and T-crossing into account. The FM generates significantly less precise results than with the RM presented in this paper.

Figs. 9 and 10 presents a comparison between the amplitude of the measured circulating currents and the computed ones using different computational models: 1) Rectangular model [RM - This Work]; 2) Filament model [FM - Ref. [2]]; 3) Resistive circuit [R only]; 4) Resistive circuit with additional elements [R only w/ add]. The FM generates outliers due to the position of the return conductor. Moreover, the FM exhibits significantly higher differences with the measurements compared to the other models and will, therefore, be left out for further comparisons. The ”R only w/ add” has a slightly better match with the measurements, exhibiting a Poisson distribution of the differences. However, this primitive model cannot predict the phase of the currents. The phase shift in the currents is depicted in Fig. 6.

Fig. 11 assesses the measured circulating currents the proposed Rm with and without resistive adds. It must be emphasized that the RM with additional elements generates in

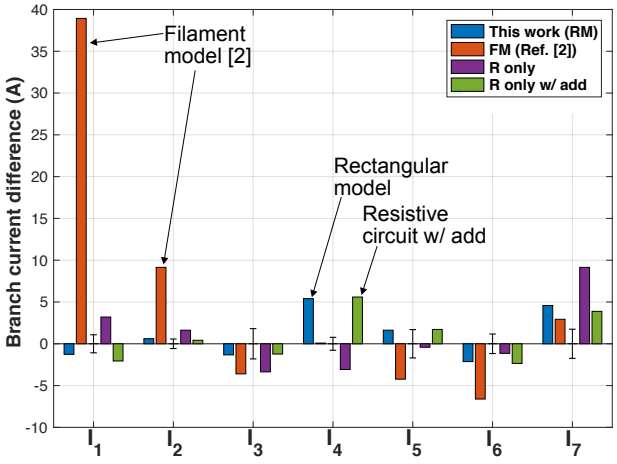

Fig. 10: Straight circuit: Bar graph of the difference between each model and the measured current amplitude of each branch.

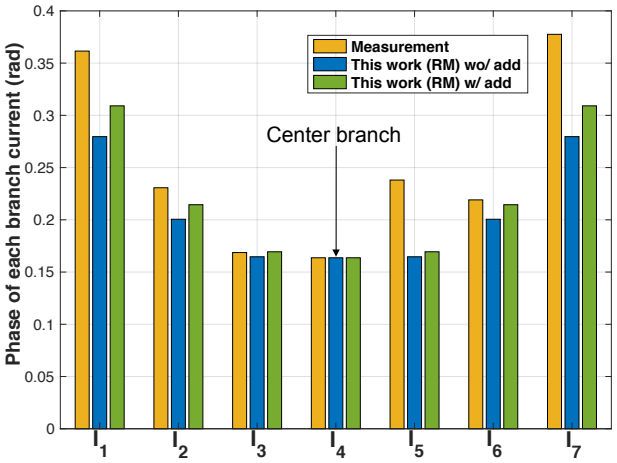

Fig. 11: Straight circuit: Bar graph of the branch current phase for different models (phase of source as reference).

all cases a smaller difference to the measurements. It seems that the phase error increases with increased distance from the current feeding point (as also highlighted in Table V). The main results show that the additional elements have a positive impact on the calculation of both the amplitude and the phase shift on the computed circulating currents.

D. Additional Considerations from the Arced Circuit

Fig. 12 depicts the main results from the investigations of the arced circuit. Without any additional resistance, only two branch currents are inside the measurement tolerance (neglecting branch 6 due to its significant error). With the additional resistances, four branch currents are inside, and the last two are much closer to the measurements. As a result, the positive impact of the additional elements into the RM model is demonstrated.

Fig. 13 presents a similar assessment of the arced circuit as for the straight circuit in Fig. 10. The additional elements reduced the difference between the computed and the measured amplitudes significantly.

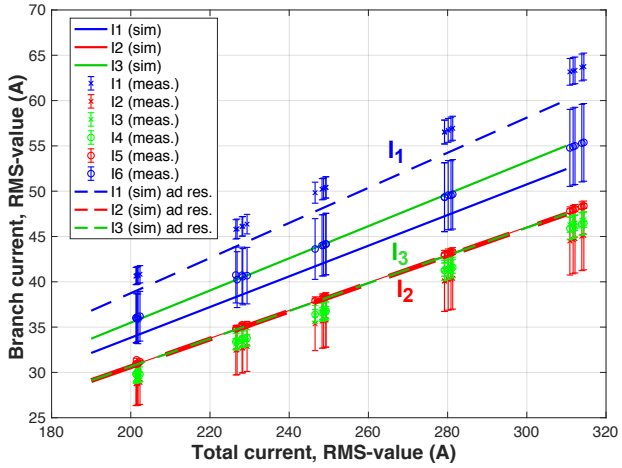

Fig. 12: Arced circuit: Branch current vs Total current, due to symmetry reasons only the different simulated currents are plotted (for example I1=I6 and so on).

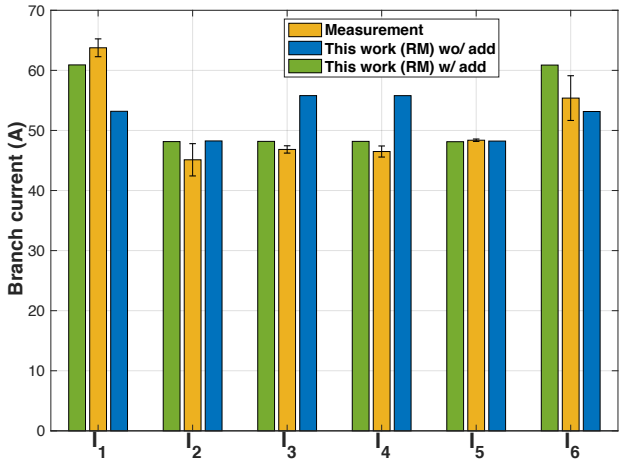

Fig. 13: Arced circuit: Bar graph of the branch current amplitude comparison of different computation models.

V. Conclusion

This paper presents and validates a novel winding overhang strand inductance model that takes the strand dimensions and bar bending into account and get rid of the return conductor. A comparison with existing models shows its significant enhancement in numerical precision. The opportunities and limitations of the lumped-element model (LEM) have been demonstrated experimentally in the small-scale case. In our case, the dimensions of the connection point are comparable to the strand dimensions. Additional parasitic resistance elements have been proposed and validated experimentally to increase the domain of use of LEMs in circulating current prediction of AC machines.

The experimental setup highlights the importance of precise and complete inductive-resistive model to achieve a high fidelity agreement between the measurements and the simulations. In fact, the circulating current calculation is nothing else than a short-circuit current calculation. Moreover, the skin effect and the proximity effect may also impact the

measurement. However, this effect was not quantified in detail for this contribution. Future efforts will handle the remaining peculiarities and differences between the simulation and the measurement. One approach would be to work on other LEM-based extensions. Moreover, a second generation of an arced conductor experimental device having longer arc-lengths will be designed to obtain better results for arc-shaped segments.

REFERENCES

[1] M. A. Iseli, "Zusatzverluste in statorwicklungen grosser synchronmaschinen unter berücksichtigung der verdrillung und der stirnraumfelder," Ph.D. dissertation, ETH Zurich, 1991.

[2] J. Haldemann, "Untersuchung verschiedener verdrillungsarten in statorwicklungen großer synchronmaschinen, deren wirkung auf strom- und temperaturverteilung und zusatzverluste in verschiedenen betriebszuständen," Ph.D. dissertation, ETH Zurich, 1997.

[3] Tang Renyuan, Xu Guangren, Tian Lijian, Zhao Danqun, and Xu Yi, "Calculation of end region magnetic field and circulation losses for turbo-generators using a coupled field and circuit equations method," *IEEE Trans.Magn.*, vol. 26, no. 2, pp. 497–500, March 1990.

[4] M. Fujita, Y. Kabata, T. Tokumasu, K. Nagakura, M. Kakiuchi, and S. Nagano, "Circulating currents in stator coils of large turbine generators and loss reduction," *IEEE Trans. Ind. Appl.*, vol. 45, no. 2, pp. 685–693, March 2009.

[5] J. Zou, B. Zhao, Y. Xu, J. Shang, and W. Liang, "A new end windings transposition to reduce windings eddy loss for 2 mw direct drive multi-unit pmsm," *IEEE Trans. Magn.*, vol. 48, no. 11, pp. 3323–3326, Nov 2012.

[6] Y. Liang, X. Bian, H. Yu, L. Wu, and L. Yang, "Analytic algorithm for strand slot leakage reactance of the transposition bar in an ac machine," *IEEE Trans. Ind. Electron.*, vol. 61, no. 10, pp. 5232–5240, Oct 2014.

[7] Y. Liang, X. Bian, L. Yang, and L. Wu, "Numerical calculation of circulating current losses in stator transposition bar of large hydro-generator," *IET Sci. Meas. Technol.*, vol. 9, no. 4, pp. 485–491, 2015.

[8] Y. Liang, L. Wu, X. Bian, and H. Yu, "The influence of transposition angle on 3-d global domain magnetic field of stator bar in water-cooled turbo-generator," *IEEE Trans. Magn.*, vol. 51, no. 11, pp. 1–4, Nov 2015.

[9] Y. Liang, X. Bian, H. Yu, L. Wu, and B. Wang, "Analytical algorithm for strand end leakage reactance of transposition bar in ac machine," *IEEE Trans. Energy Convers.*, vol. 30, no. 2, pp. 533–540, June 2015.

[10] X. Bian, Y. Liang, and G. Li, "Analytical algorithm of calculating circulating currents between the strands of stator winding bars of large turbo-generators considering the air gap magnetic field entering stator slots," *IEEE Trans. Energy Convers.*, vol. 33, no. 1, pp. 32–39, March 2018.

[11] X. Bian and Y. Liang, "Circuit network model of stator transposition bar in large generators and calculation of circulating current," *IEEE Trans. Ind. Electron.*, vol. 62, no. 3, pp. 1392–1399, March 2015.

[12] Y. Liang and Y. Chen, "Circulating current losses analysis and improved incomplete transposition for stator bars in large hydro-generators," *IET Elect. Power Appl.*, vol. 10, no. 2, pp. 125–132, 2016.

[13] Y. Liang, L. Wu, X. Bian, and C. Wang, "Influence of void transposition structure on the leakage magnetic field and circulating current loss of stator bars in water-cooled turbo-generators," *IEEE Trans. Ind. Electron.*, vol. 63, no. 6, pp. 3389–3396, June 2016.

[14] J. Haldemann, "Transpositions in stator bars of large turbogenerators," *IEEE Trans. Energy Convers.*, vol. 19, no. 3, pp. 553–560, Sep. 2004.

[15] C. Wang, Y. Liang, X. Bian, and Y. Wan, "Measuring method for strand current of stator bars based on search coils," *IEEE Trans. Ind. Electron.*, vol. 66, no. 9, pp. 7347–7355, Sep. 2019.

[16] X. Bian, Y. Liang, C. Wang, D. Wang, and L. Gao, "Influence of stator end structures on the end leakage magnetic field for stator bars in large turbo-generators," in *Proc. Int. Conf. on Elect. Mach. Syst.*, Aug 2019, pp. 1–4.

[17] X. Bian and Y. Liang, "Analysis on eddy current losses in stator windings of large hydro-generator considering transposed structure based on analytical calculation method," *IEEE Access*, vol. 7, pp. 163 948–163 957, 2019.

[18] J. Haldemann, "Stator winding of a directly cooled turbogenerator," Jul. 4 2017, US Patent App. 9,698,640.

[19] R. Wrobel, A. Mlot, and P. H. Mellor, "Contribution of end-winding proximity losses to temperature variation in electromagnetic devices," *IEEE Trans. Ind. Electron.*, vol. 59, no. 2, pp. 848–857, Feb 2012.

[20] A. Lehikoinen and A. Arkkio, "Efficient finite-element computation of circulating currents in thin parallel strands," *IEEE Trans. Magn.*, vol. 52, no. 3, pp. 1–4, March 2016.

[21] A. Lehikoinen, N. Chiodetto, E. Lantto, A. Arkkio, and A. Belahcen, "Monte carlo analysis of circulating currents in random-wound electrical machines," *IEEE Trans. Magn.*, vol. 52, no. 8, pp. 1–12, Aug 2016.

[22] C. Wang, Y. Liang, L. Ni, D. Wang, and X. Bian, "Calculation and analysis of the strands short-circuit in stator transposition bar for large generators," *IEEE Access*, vol. 7, pp. 36 132–36 139, 2019.

[23] S. E. Dallas, A. N. Safacas, and J. C. Kappatou, "Interturn stator faults analysis of a 200-mva hydrogenerator during transient operation using fem," *IEEE Trans. Energy Convers.*, vol. 26, no. 4, pp. 1151–1160, Dec 2011.

[24] R. Romary, C. Demian, P. Schlupp, and J. Roger, "Offline and online methods for stator core fault detection in large generators," *IEEE Trans. Ind. Electron.*, vol. 60, no. 9, pp. 4084–4092, Sep. 2013.

[25] "Electrical effects in winding of large electrical ac machines application to advanced large size DFIM," Ph.D. dissertation. [Online]. Available: https://infoscience.epfl.ch/record/265156?ln=fr

[26] W.-R. Novender, *Dreidimensionale nichtlineare Magnetfeld-Berechnung für Synchron-Turbogeneratoren zur Bestimmung der Schlingstromverteilung in Roebelstäben*. PhD Thesis - TH Darmstadt, 1984.

[27] P. Roshanfekr Fard, "Roebel windings for hydro generators," Master's thesis, Chalmers University of Technology, 2007.

[28] C. R. Paul, "Partial inductance," in *Proc. IEEE Int. Symp. Electromagn. Compatibil.* IEEE, 2008, pp. 1–23.

[29] C. R. Paul, "What is partial inductance?" in *Proc. IEEE Int. Symp. Electromagn. Compatibil.*, Aug 2008, pp. 1–23.

[30] H. A. Aebischer and B. Aebischer, "Improved formulae for the inductance of straight wires," *Advanced Electromagnetics*, vol. 3, no. 1, pp. 31–43, 2014.

[31] D. M. Beams and S. G. Annam, "Calculation of mutual inductance from magnetic vector potential for wireless power transfer applications," in *Proc. Southeast. Symp. Syst. Theory*, March 2012, pp. 209–213.

[32] L. Urankar, "Vector potential and magnetic field of current-carrying finite arc segment in analytical form, part iii: Exact computation for rectangular cross section," *IEEE Trans. Magn.*, vol. 18, no. 6, pp. 1860–1867, November 1982.

[33] F. Maurer, B. Kawkabani, and J. Nøland, "Rapid 3-D magnetic integral field computation of current-carrying finite arc segments with rectangular cross section," *IEEE Trans. Magn.*, vol. 99, no. PP, pp. 1–12, 2020.

Frederic Maurer received his master degree in 2009 and the Ph.D. degree in 2019 from the Swiss Federal Institute of Technology in Lausanne (EPFL). Since april 2009, he is working for Alstom Hydro (now GE Hydro) in different position: R&D engineer in the generator technology center, Lead electrical engineer and technical project manager.

Jonas Kristiansen Nøland (S'14-M'17) received the Ph.D. degree in engineering physics from Uppsala University, Uppsala, Sweden, in 2017. He is currently an Associate Professor with the Department of Electric Power Engineering, Norwegian University of Science and Technology (NTNU), Trondheim, Norway. He has been actively involved in the grid standardization of new excitation system technologies. His current research interests include excitation systems, improved utilization of electrical machines, high-power machinery for aircraft applications, as well as transportation electrification in general.

Dr. Nøland currently serves as an Editor for the IEEE TRANSACTIONS ON ENERGY CONVERSION. He is a Board Member of the Norwegian Academic Committee of Publication in Technology and a Vice-Chair of the IEEE Power and Energy Chapter of Norway. He is also a member of the IEEE Transportation Electrification Community (TEC), IEEE Industrial Electronics Society (IES), the IES Electric Machines Technical Committee, the IEEE Industry Applications Society (IAS), and the IEEE Power and Energy Society (PES).